ADVANCED ENERGY MATERIALS
www.advenergymat.de

In–Li Counter Electrodes in Solid-State Batteries – A Comparative Approach on Kinetics, Microstructure, and Chemomechanics

*Christoph D. Alt, Sören Keuntje, Inga L. Schneider, Johannes Westphal, Philip Minnmann, Janis K. Eckhardt, Klaus Peppler, and Jürgen Janek**

A key challenge for solid-state batteries is the fabrication of high-capacity cathodes with high area loading and good rate performance. To reliably quantify the performance of high-capacity cathodes, electrochemically stable, and high-rate counter electrodes are essential. Otherwise, a three-electrode setup is required. In–Li alloy electrodes are used for years in a kind of standard approach, since these seem to offer stable operation. In this comparative study, seven preparation methods for In–Li electrodes are examined, determining their suitability for cathode testing. The microstructure of a planar (i.e., foil) and a particle-based (i.e., composite) anode configuration is analyzed in more detail. Their rate-dependent electrode performance as well as electrochemical and chemomechanical reversibility in full-cell configuration are analyzed. The combined results demonstrate the limitations of In–Li electrodes for high-capacity testing, especially at high rates, while confirming their suitability for simple lab-scale testing. Preparation significantly influences the electrode microstructure and kinetics, consequently impacting the performance benchmarks of cathodes. These findings underscore both the challenges involved in applying In–Li counter electrodes and the resulting limited comparability of results from different laboratories.

1. Introduction

With the ongoing shift from combustion-based mobility to sustainable electric transportation, high-energy solid-state batteries (SSB) have garnered significant interest in recent years.[1,2] Inorganic solid electrolytes (SE) offer the possibility to employ lithium metal anodes (LMA) and high-capacity cathode composites, allowing SSBs theoretically to exceed the performance of conventional lithium ion batteries (LIB), which are slowly approaching physicochemical limitations.[3–5] Hence, SSBs are anticipated to offer high power and energy densities, while ensuring safe and reliable operation.[6–10]

In order to fully utilize high-capacity cathode active materials (CAM), which can provide area loadings of up to 10 mAh cm^{-2}, an optimized cathode microstructure with high-rate capability is required.[11,12] Additional issues such as chemomechanical volume changes and related CAM particle cracking need to be addressed.[13,14] For optimization efforts, cathode performance must be quantified reliably, and any effects introduced by deficient counter electrodes (CE) in two-electrode cell setups should be avoided.[15–17] The best way to achieve this is the use of reference electrodes (RE) in three-electrode (3E) setups. This has not been widely reported yet – mostly due to the difficulties in incorporating REs in SSB cells. Miniaturization and geometric challenges (i.e., RE positioning) as well as proper material selection to avoid both SE degradation and reference potential fluctuations, hinder its widespread adoption in SSBs.[18,19] However, first successful integrations of REs have recently been reported. Various approaches like lithiated metal meshes or wires (i.e., out of indium, gold, or silver)[20,21] have been utilized, even achieving µ-REs. Morphological and chemical stability issues (i.e., SEI formation) inhibit the use of lithium metal itself with thiophosphate-based SEs.[22,23]

To avoid the difficulties posed by 3E configurations and reduce preparation requirements, it is essential to introduce electrochemically stable CEs with high rate capability and low overpotential (i.e., defined and stable half-cell potential, favorable kinetics, and reversibility).[16] The binary In–Li alloy system offers

C. D. Alt, S. Keuntje, I. L. Schneider, J. Westphal, P. Minnmann, J. K. Eckhardt, K. Peppler, J. Janek
Institute of Physical Chemistry
Justus Liebig University
Heinrich Buff Ring 17, 35392 Giessen, Germany
E-mail: juergen.janek@phys.chemie.uni-giessen.de

C. D. Alt, S. Keuntje, I. L. Schneider, J. Westphal, P. Minnmann, J. K. Eckhardt, K. Peppler, J. Janek
Center for Materials Research
Justus Liebig University
Heinrich Buff Ring 16, 35392 Giessen, Germany

J. K. Eckhardt
Institute for Theoretical Physics
Justus Liebig University
Heinrich Buff Ring 16, 35392 Giessen, Germany

The ORCID identification number(s) for the author(s) of this article can be found under https://doi.org/10.1002/aenm.202404055

DOI: 10.1002/aenm.202404055

a range of advantageous attributes, is well-known for its potential plateaus, and has been early introduced in the study of SSB test cells.[24–28] Especially, the two-phase eutectic $In/(InLi)_x$ provides a stable potential of E_H(vs Li^+/Li) = 0.62 V over a wide stoichiometry range (≈1–47 at.% of lithium).[19,29] Degradation of thiophosphate-based SEs is anticipated to be minor at this potential. However, recent findings suggest the emergence of In_xS_y compounds at the interface with the $In/(InLi)_x$ eutectic.[30,31] Notably, Qu et al.[32] and Hänsel et al.[33] have examined the lithium transport properties of various In–Li phases, highlighting fast lithium migration attributed to low activation barriers. Accordingly, the fast diffusion kinetics (D_{Li} = 10^{-8}–10^{-7} cm^2 s^{-1} of the intermetallic InLi phase) are promising to ensure good electrochemical performance and stable SSB cycling.[34–36] In comparison to lithium metal, the volume expansion of indium up to the intermetallic InLi phase of 105 % is lower.[37] Intimate interfacial contact due to the ductile character of indium metal[33,34] enables a low interfacial impedance[29] as well as good local current distribution to provide uniform lithium deposition and dissolution.[34,35,38] To the best of our knowledge, fatal morphological changes of In–Li anodes have only been reported once (after 900 cycles at 3.8 mA cm^{-2} and 150 MPa).[30]

The large-scale application of indium-based electrodes is impeded by raw material costs, interest of other technology sectors, and scarce availability.[39] Nevertheless, the In–Li anode is commonly selected by researchers as a stable CE for lab-scale purpose.[40–42] A significant capacity decay is observed due to the lithiation and alloying if pure indium metal is used as an electrode (shown in Figure S1 and Section SA, Supporting Information). Thus, lab-scale In–Li anodes are mostly manufactured either by stacking (and pressing) indium and lithium metal foils or by mixing metal powders of both alloying components. More complex geometries or pre-lithiation approaches are used less frequently.[34,43] Santhosha et al.[19] demonstrated the benefits of a centrally-located composition within the two-phase eutectic $In/(InLi)_x$. While Wang et al.[36] suggest 14.3 at.% lithium as optimum for fast kinetics, Yanev et al.[44] investigated the boundaries of this phase field up to lithium contents of 50 at.%, and compare three different types of electrode preparation. Hänsel et al.[33] reported kinetic limitations for the (higher lithitated) intermetallic In_3Li_{13} phase.

Summarizing various reports in the literature, In–Li anodes suffer from being mechanically stiffer – compared to pure indium – due to the mechanical properties of the InLi phase (Young's modulus of 46.1 GPa and hardness of 1.82 GPa).[34] Moreover, insufficient electrode kinetics during cycling appear to be associated with the specific preparation of the anode eutectic.[16] To the best of our knowledge, Ikezawa et al.[41] and Nam et al.[16] were the first to report sluggish electrode performance and kinetics using foil type In–Li electrodes. In their study, Nam et al. suspect lithium-deficient layers at the interface between the InLi intermetallic and the SE, thus, identify lithium transport in InLi intermetallic as a bottleneck. Wang et al.[36] and Aspinall et al.[34] provided evidence of the evolution of indium-rich layers in In–Li anodes after discharge processes through microstructural analysis, utilizing electron microscopy and X-ray computed tomography, respectively. Further, Sedlmeier et al.[45] demonstrated the negative effects of $In/(InLi)_x$ phase inhomogeneities by testing thick indium foils (facing toward the SE).

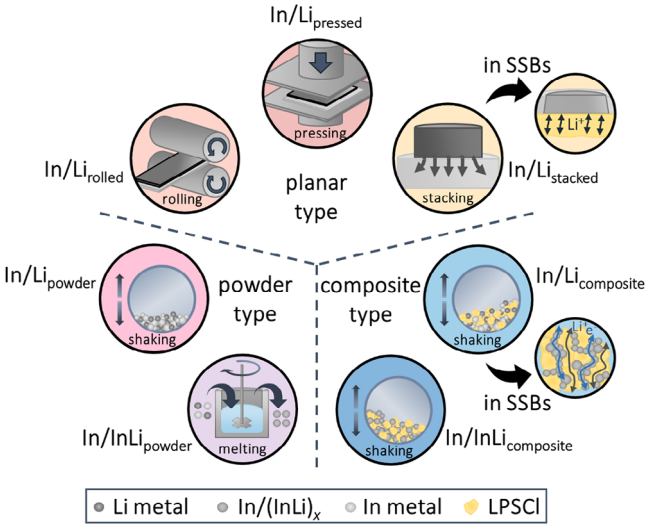

Figure 1. Illustration of the preparation methods tested. For the extensively studied types, namely $In/Li_{stacked}$ and $In/Li_{composite}$, illustrations of their structure and application in SSBs are included. Please note that the dimensions of foils and particles are not necessarily to scale.

However, their approach of contacting first lithium metal with the SE, before the formation of the eutectic will cause severe SE degradation. Nam et al.[16] improved electrode kinetics and rate capabilities by introducing In–Li anode composites including SE particles. This approach aimed to establish ionic percolation paths and reduce the reliance on diffusion within the intermetallic phase. This has recently been confirmed by Yanev et al.[44] through a concise and systematic set of performance studies, clearly recommending the composite approach, once no RE is being used.

While these studies are valuable and individually improve the understanding of single In–Li alloy electrodes, a comparative study is missing. The rate-dependent performance and the underlying microstructure of various In–Li eutectics during repetitive cycling has not been thoroughly investigated or understood yet. This clearly compromises the reliable benchmarking of cathode composites under relevant test conditions and, consequently, the interlaboratory comparability of results.[46]

In this work, we therefore examined several reported and feasible In–Li eutectic preparation methods regarding their suitability for lab-scale utilization as CEs in the investigation of solid-state cathodes. We compared five different In–Li eutectic preparations and two electrode composites, as shown in **Figure 1**. To better understand the inconsistent performances between different electrode types, we complement our detailed electrochemical analysis with results on microstructure and chemomechanics, aiming to establish appropriate selection criteria. Unidirectional galvanostatic experiments reveal the intermixing during preparation and the kinetic limitations (i.e., lithium accessibility) of each type of anode. To fully describe the electrode performance of the most effective preparations methods, namely planar $In/Li_{stacked}$ and particle-based $In/Li_{composite}$, we prepared cross sections to analyze their microstructure using scanning electron microscopy (SEM) and electron backscatter diffraction (EBSD). The analysis of volume changes in planar and particle-based electrodes,

along with the study of their electrode kinetics (i.e., reversibility and overpotentials) in full-cell configuration, were used to evaluate their integration as stable CEs. It reveals the individual performance, benefits, and bottlenecks of both electrode types concerning high-capacity cathode benchmarking. Conclusively, this work highlights the challenges and consequences of variations in preparation procedures across different laboratories.

2. Results

$In/(InLi)_x$ electrodes were prepared using different methods and can be divided into three groups: 1) planar (i.e., foils), 2) powder, and 3) composite type. Figure 1 illustrates each preparation method. The lithium content was set at 35 at%, which is centrally located in the two-phase region $In/(InLi)_x$. This ensures comparability across all preparation methods. The planar electrodes used are denoted as "In/Li_{rolled}", "$In/Li_{pressed}$", and "$In/Li_{stacked}$". Powder electrode types are referred to as "In/Li_{powder}" and "$In/InLi_{powder}$" for blended or fused (i.e., alloyed) powders, respectively. In–Li alloy composite anodes were prepared from both powder type electrodes and Li_6PS_5Cl (LPSCl), with the resulting materials labeled "$In/Li_{composite}$" and "$In/InLi_{composite}$", respectively.

At this point, we like to acknowledge that the terms "negative" and "positive" electrode should be used to address both electrodes correctly. To align with commonly used terminology, we use the terms "anode" and "cathode".

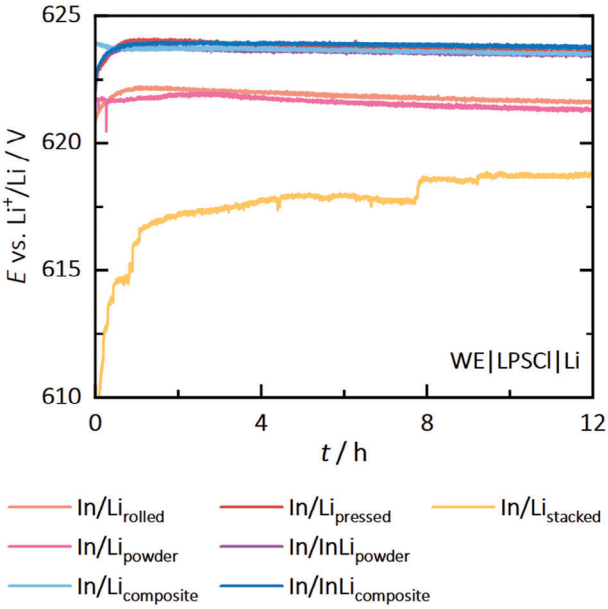

Figure 2. Results of OCV measurements for each In–Li anode (WE | LPSCl | Li). The potential (vs Li^+/Li) is recorded for 12 h after electrode preparation, measured at 25 °C, and and 30 MPa. A single cell was tested for each In–Li anode.

2.1. Equilibration of In—Li Alloy Electrodes After Preparation

The electrode potential was monitored for 12 h by recording the open-circuit voltage (OCV) of $In/(InLi)_x$ | LPSCl | Li cells (**Figure 2**). During the alloying process, lithium metal is consumed, forming the intermetallic compound InLi, which establishes the characteristic potential of the two-phase eutectic $In/(InLi)_x$ at 0.62 V (vs Li^+/Li). The electrodes are initially not in equilibrium, as indicated by the changing potential. Once a stable potential is reached, equilibrium is achieved. However, even a small amount of residual lithium metal within the WEs would prevent complete equilibration, causing the electrode potential to continue changing over time. Therefore, the successful completion of the alloying process (i.e., complete consumption of lithium metal) is confirmed by achieving a stable potential. In/Li_{rolled} (light red) and $In/InLi_{powder}$ (violet) exhibit a potential of ≈622 mV, while $In/Li_{pressed}$ (dark red), In/Li_{powder} (light violet), $In/Li_{composite}$ (light blue), and $In/InLi_{composite}$ (blue) show potentials of ≈623 mV. Each potential stabilizes within less than 1 h. In the case of $In/Li_{stacked}$ (yellow), relying on long-range lithium diffusion into the indium foil (100 µm thick), a stable potential of ≈618 mV is achieved only after 8 – 10 h. Hence, the utilization of $In/Li_{stacked}$ is inevitably associated with a transient period of several hours prior to electrochemical application.

2.2. Performance in Cell Configurations with Two In—Li Electrodes

The primary cause of dendrite formation and cell failure in SSBs with LMAs is current constriction due to void formation at the stripped lithium electrode.[34,47,48] Accordingly, the as-prepared In–Li electrodes are first evaluated in delithiation experiments. Based on their accessible lithium capacity ($q_{th,delith}$ = 8.4 mAh cm^{-2}), their degree of "bulk" alloying (i.e., intermixing) and suitability for SSB cell testing is approximated.

Figure 3 illustrates the potential profiles (vs $In/(InLi)_x$) for unidirectional galvanostatic stripping at 0.5 mA cm^{-2} in WE | LPSCl | $In/Li_{stacked}$ configuration, referenced to the $In/Li_{stacked}$ CE. With the exception of $In/Li_{pressed}$, each In–Li anode displays initially flat profiles with low potential increases during ongoing lithium stripping, before a steep potential rise indicates lithium depletion.[49] Further discussion on the origin of polarization through analysis of impedance and microstructure is provided below. Clearly, an increasing overpotential caused by polarization affects the overall cell performance and indicates a limitation for the use in high-capacity cell testing.

The accessible capacity (i.e., the amount of extractable lithium) at which polarization initiates varies among the preparation methods. The observed variation is 1) attributed to the degree of intermixing during preparation, which determines the initial spatial distribution of lithium within the electrode, and 2) lithium replenishment properties (governed by diffusion). Consequently, this capacity serves as a key indicator for the suitability of each In–Li electrode type for their use as CE in SSB test cells. We define reliable capacities for each electrode type based on the point where significant polarization (>100 mV) initiates and refer to it as q_{exp}. This value is defined as a threshold, as we consider overpotentials exceeding 100 mV as too high, particularly in full-cells (i.e., during the charging process), as discussed below. Further, we define the lithium accessibility, denoted as $\xi_{exp} = q_{exp}/q_{th} \cdot 100\,\%$, to compare the effective accessible capacities during lithium stripping of a pristine electrode.

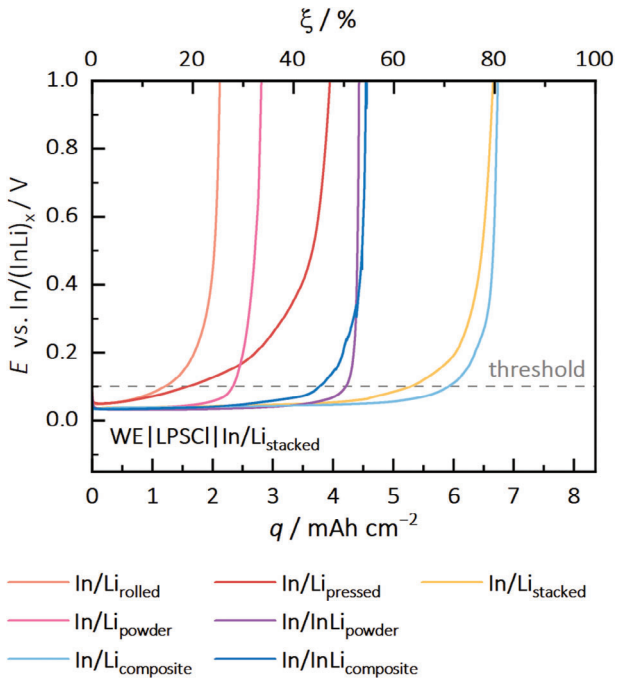

Figure 3. Results of delithiation experiments of each In–Li anode (WE | LPSCl | In/$Li_{stacked}$). Potential profiles (vs In/$(InLi)_x$) for unidirectional galvanostatic stripping at 0.5 mA cm^{-2}, 25 °C, and 30 MPa were recorded until the cut-off potential of 1 V was reached. The threshold of 100 mV is indicated in gray. Stable potentials and low overpotentials up to capacities of 5.9 mAh cm^{-2} indicate the high lithium accessibility within In/$Li_{stacked}$ and In/$Li_{composite}$ (represented in light blue and yellow, respectively). A comparison of the accessible capacities q_{exp} is provided in Figure S3 (Section SB, Supporting Information), including averages and standard deviations for In/$Li_{stacked}$ and In/$Li_{composite}$ for a total number of three cells.

For In/Li_{rolled} and In/$Li_{pressed}$, accessible capacities of approximately q_{exp} = 1.2 and 1.6 mAh cm^{-2} were observed before severe polarization began, corresponding to $\xi_{exp} \approx 20\%$. This suggests that mechanical mixing through folding and compressing of foils is difficult to control, resulting in inadequate homogenization and uncontrolled microstructure of the eutectic. Consequently, the properties of these electrode foils are significantly influenced by the specific area (i.e., local composition) designated for use. As reported in the experimental section, the prepared alloy foils became stiff, which is an indication of the intermetallic InLi phase. The stiff nature of these alloyed foils impairs the contact at the interface with the SE.[34] In contrast, the soft indium layer used for the preparation of In/$Li_{stacked}$ provides a better contact at the interface. Accordingly, In/$Li_{stacked}$ exhibited a higher capacity of q_{exp} = 5.2 mAh cm^{-2} (ξ_{exp} = 60%), establishing itself as the most effective anode type among the three planar anode types.

q_{exp} of 2.3 and 4.2 mAh cm^{-2} were accessed from In/Li_{powder} and In/$InLi_{powder}$, corresponding to ξ_{exp} = 27% and 49%, respectively. This suggests insufficient lithium mobility caused by the solid-state transport of lithium within both metallic composites, particle-particle boundaries, and pores. By adding LPSCl to the mixture, ionic percolation paths are introduced, the intermetallic transport pathlength decreased, and kinetic limitations reduced.[16,29] Hence, this enhances the accessible lithium capacity (from deeper regions of the electrode) to q_{exp} = 3.8 and 5.9 mAh cm^{-2} for In/$InLi_{composite}$ and In/$Li_{composite}$, corresponding to ξ_{exp} = 44% and 69%, respectively. Hence, increasing the effective lithium mobility demonstrates the advantage of the composite-type electrode. In/$Li_{composite}$, composed of lithium and indium powder combined with LPSCl, is the most useful concept among the particle-based electrodes.

Figure S3 (Section SB, Supporting Information) presents a comparison of the accessible capacities (q_{exp}), including averages and standard deviations for In/$Li_{stacked}$ and In/$Li_{composite}$ with data derived from three cells each. The statistical analysis yields q_{exp} values of (5.00 ± 0.21) and 5.62 ± 0.29) mAh cm^{-2}, respectively. This highlights satisfactory reproducibility for both of these promising electrodes for further in-depth investigation. Please note that only a single cell was tested for the other, less promising electrode types.

Effective capacities of up to ξ_{exp} = 69%, approaching the theoretical lithiation capacity of the In/$Li_{stacked}$ CE, were achieved. This demonstrates comparable or even higher lithium accessibility to the data reported by Aspinall et al.[34] As a preliminary conclusion, it is apparently not trivial to prepare In–Li anodes with high lithium accessibility. Careful preparation of In–Li eutectic anodes is crucial for mitigating property variations among electrodes prepared in different laboratories, ultimately ensuring consistent performance and facilitating comparable results. Therefore, this emphasizes the necessity for interlaboratory studies, more comprehensive reports of experimental details in literature, and transparent analysis.[46,50]

To evaluate the electrode kinetics for studying high cathode capacities in greater detail, both In/$Li_{stacked}$ and In/$Li_{composite}$ were tested at rates ranging from 0.25 to 5 mA cm^{-2} in symmetric cells with In/$Li_{stacked}$ CEs (see Figure S4, Section SC, Supporting Information). Similar to earlier findings, flat profiles with minimal potential increase during continuous lithium stripping are observed for both anode types at current densities up to 1.5 mA cm^{-2}. These rates are considered sufficient for investigating current lab-scale cathode composites for SSBs with capacities up to 1.5 mAh cm^{-2} at 1C. On the one hand, the trend of increasing overpotential indicates unsuitable performance starting around 1.5 mAh cm^{-2}, which becomes apparent at higher rates, e.g. 5 mA cm^{-2}. This exposes challenges related to sluggish kinetics and inadequate lithium transport from pre-lithiated regions of the stripped WE at high-rate testing. Notably, the potential advantages of the composite type anode (i.e., as a larger contact area and distributed lithium nucleation spots) were not clearly observed in these tests.

Plating experiments of In/$Li_{composite}$ were further conducted to comprehensively analyze its lithiation performance, which is presented in Figure S5 (Section SD, Supporting Information). Both In–Li anode types (with In/$Li_{stacked}$ serving as CE in Figure 3 and Figure S3, Supporting Information) show high effective capacities of lithium and insignificant dendrite susceptibility. Lithiation capacities close to the theoretical capacity ($q_{th,lith}$ = 7 mAh cm^{-2}) were achieved. Hence, we assume that the substantial thermodynamic barrier arising from the high alloying potential of In/$(InLi)_x$ (0.62 V vs Li^+/Li) hinders lithium metal plating and, thus, filament growth and cell shorting. These findings suggest favorable lithiation kinetics compared to our delithiation results. Further, this emphasizes the focus on improving the lithium stripping capabilities of In–Li electrodes to

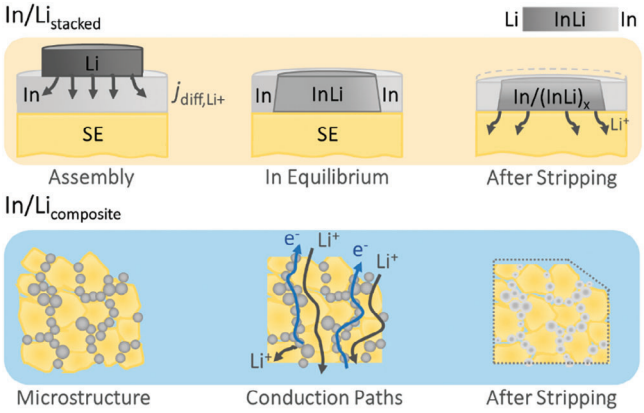

Figure 4. Schematic overview of In/$Li_{stacked}$ (top) and In/$Li_{composite}$ (bottom) electrodes on the cell level. The assembled anode (left) and anticipated equilibrium state (middle) of In/$Li_{stacked}$ are presented, while the microstructure (left) and conduction paths of both charge carriers (middle) in In/$Li_{composite}$ are illustrated. The right side displays the stripped state during lithium depletion conditions for both electrodes. Illustration of foils and particles are not necessarily to scale.

facilitate long-term testing (Figure 3). The enhanced lithium transport properties within the In/$(InLi)_x$ phase field can also be observed when compared to pure indium foil. This is shown in Figure S2 (Section SA, Supporting Information). Consequently, the pre-lithiation of indium, corresponding to the InLi phase formation, proves to be advantageous for enhancing kinetics.

2.3. Microstructural Analysis of Selected In–Li Eutectic Anode Types

We selected In/$Li_{stacked}$ and In/$Li_{composite}$ for further detailed investigation, as these demonstrated the most promising stripping performance and highest reproducibility. This selection is in line with the study of Yanev et al.[44] Consequently, these two electrodes were tested in a greater number of cells, as the other electrode concepts were less suitable for practical applications. The remaining concepts, as prepared for this study, showed insufficient intermixing, inferior stripping performance, or inadequate reproducibility and required optimization. Hence, these anodes may not be adequate CEs to ensure comparable results due to preparation inconsistencies, impeding the independent evaluation of cathode performance in SSBs. To evaluate the mechanism behind the capacity limitations, **Figure 4** first gives a schematic overview of In/$Li_{stacked}$ for planar (top) and In/$Li_{composite}$ for composite type anodes (bottom).

For In/$Li_{stacked}$, lithium atoms diffuse from the smaller lithium foil into the indium foil to form the intermetallic InLi phase (left), i.e., a diffusion-formed "bulk" eutectic. Applied pressure avoids loss of contact during interdiffusion. The two-phase region In/$(InLi)_x$ evolves with an inner core of InLi (≈7.5 mm in diameter) and an outer region of remaining indium, see Figure 4 (top, middle). Incomplete (in-depth) alloying may lead to a deficiency of the InLi phase (i.e., reduced lithium accessibility) at the interface with the SE and cause constriction effects,[44,45] which may become negligible after a first lithiation process. We like to emphasize that it is not only feasible, but important, to position the indium foil between the SE and lithium metal during the alloying process. Otherwise, early SE degradation (i.e., SEI formation) would result from the low potential of lithium metal.

In the case of In/$Li_{composite}$, the 3D phase network comprises intermetallic InLi and indium particles, distributed within the LPSCl microstructure (left). Different paths enable ion and electron transport (bottom, middle), and lithium dissolution/deposition occurs spatially distributed. However, due to the instability of thiophosphate-based SEs, it is important to consider the increased interface area between InLi and LPSCl particles within composites. More lithium will be consumed in side reactions and SEI will form due to the large contact area within the composite, potentially increasing the electrode impedance. We can assume that the volume change of the electrode is stabilized and reduced by the 3D electrolyte "scaffold" (right). This could offer a significant advantage for its use as a CE and for operation under varying stack pressures. After the initial compression during cell fabrication, the immediate contact between the electrode active material and the SE could make it a suitable choice for cell testing (e.g., in pouch cells) at ambient to low external pressures. As indium-based anodes will not be suitable for commercialization, we do not discuss further benefits, such as power density of 3D composite electrodes.[51,52] We rather emphasize the role of high-rate and high-capacity In–Li alloys as CEs in cathode tests.

In the case of In/$Li_{stacked}$, attention to the geometric ratio between the indium and lithium metal foils is crucial. We consider an incorrect choice of parameters, such as variations in composition, areal or thickness ratio, as one of the major factors contributing to decreased interlaboratory comparability. The results of delithiation experiments in Figure S6 (Section SE, Supporting Information) indicate the significant impact of different lithium metal foil thicknesses and diameters on performance. While we varied the thickness ratio between lithium and indium metal foil, we maintained the composition (i.e., volume and capacity). By comparing delithiation capacities in Figure S6 (Supporting Information), we identify an optimum for the lithium metal foil thickness of 100 µm (and 6 mm diameter) combined with 100 µm indium foil (and 9 mm diameter). We anticipate that using thinner or thicker lithium metal foils will create blocking indium layers or reduce the active area, respectively, resulting in lower effective stripping capacities. We suspect that these factors lead to reduced comparability and inaccurate conclusions across various reports in literature, especially when thinner lithium metal foil was used to match the areas of both foils during preparation.

The thickness ratio between the indium and lithium metal foil appears to be a critical factor that may hinder sufficient lithium transport in the two-phase eutectic. Accordingly, the thickness of the lithium foil should be chosen to match the dimension of the indium foil (see calculation in Section SE, Supporting Information). We suggest a thickness ratio of d_{Li}/d_{In} between 0.9 and 1 to avoid blocking indium layers, while ensuring a sufficient alloying reaction up to the interface with the SE. This also compensates for the loss of lithium inventory due to passivation reactions with the SE or trace amounts of moisture inside SSBs and during preparation. However, this suggested ratio results in the lithium foil having a smaller area than the indium foil.

For In/$Li_{composite}$, the incorporation of SE requires precise adjustment of components to increase the effective ionic conductivity, while maintaining appropriate electronic percolation paths

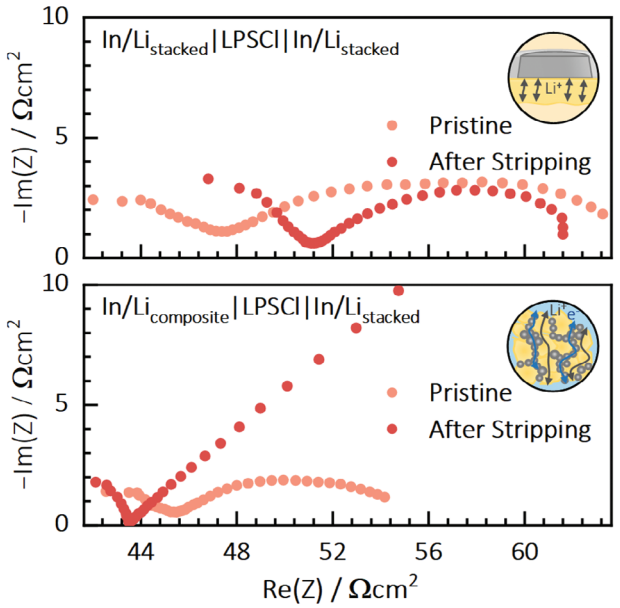

Figure 5. Results of impedance measurements of In/Li$_{stacked}$ (top) and In/Li$_{composite}$ (bottom) cells (WE | LPSCl | In/Li$_{stacked}$) during unidirectional galvanostatic stripping at 0.5 mA cm^{-2}, 25 °C, and 30 MPa with a cut-off potential of 1 V (corresponding to the same cells in Figure 3). Impedance spectra are recorded both before (pristine, light red) and after the delithiation experiment (dark red). The high impedance evolving at 43.6 Ω cm^{-2} indicates a blocking behavior (i.e., full lithium depletion) for In/Li$_{composite}$ after stripping.

within the 3D structure. It is crucial to ensure that excess SE does not obstruct the electronic percolation paths and create isolated metallic domains. At the same time, the indium particles provide sufficient electronic conductivity and contact during ongoing stripping. In our study, we carefully adjusted the volume fraction of SE and In/(InLi)$_x$, assuming complete alloying of lithium with indium and surplus indium, to be ≈64 and 36 vol%, respectively.[16] The particle sizes of the initial lithium and indium metal powder are also expected to influence percolation paths, although investigating this aspect falls outside the scope of this work.[12]

To further investigate the origin of capacity limitation, impedance spectra were recorded for both electrode types. **Figure 5** shows the impedance spectra of In/Li$_{stacked}$ (top) and In/Li$_{composite}$ (bottom) in WE | LPSCl | In/Li$_{stacked}$ configuration. Spectra were recorded both before (depicted in light red) and after (dark red) the delithiation experiments and correspond to the same cells tested at unidirectional galvanostatic stripping currents of 0.5 mA cm^{-2} in Figure 3. The initial impedance of In/Li$_{composite}$ is slightly lower compared to In/Li$_{stacked}$. We believe this is caused by the enhanced contact area between the SE and the composite electrode due to its 3D structure and densification during cell assembly. Hence, we anticipate a lower impedance for this electrode type.

At the end of the delithiation experiments, severe cell polarization is observed for both electrodes (see Figure 3). Usually, the primary reason for polarization effects (i.e., overpotentials) in SSBs with LMAs is current constriction resulting from void formation at the anode at high current densities and too low applied pressure.[47,48] In the case of In–Li anodes, lithium stripping is impeded due to concentration polarization, as discussed in detail for Li–Mg alloy anodes.[53–55] This limitation may be attributed to sluggish lithium transport and constraints (i.e., lithium deficiencies) within the respective electrode material or incomplete lithium intermixing during the preparation process. The latter applies to most of the preparation methods tested (see Figure 3).

During ongoing stripping of In/Li$_{stacked}$, pure indium precipitates (i.e., layers with a deficiency in lithium) form, as observed by Jeong et al.[42]). Later, we suspect that the electrode polarizes due to blocking properties of precipitated indium near the interface. Ultimately, this may lead to a reduction in active area, and current constriction at high depletion levels may dominate the electrode kinetics (similar to void formation in LMAs). Analyzing In/Li$_{stacked}$, the lithium flux gets insufficient after extracting high lithium capacities. Hereby, the cut-off potential of 1 V corresponds to a dc-resistance of ≈2 kΩ cm^{-2}. However, the impedance spectrum following the cut-off ("after stripping") shows an impedance of ≈61 Ω cm^{-2}. This discrepancy in resistance indicates a rapid relaxation of the electrode, suggesting that a complete lithium depletion was not achieved (i.e., small domains of InLi remain). Both OCV and impedance relaxation experiments in Figure S7 (Section SF, Supporting Information) show, that the impedance quickly recovers after the cut-off potential was reached. We like to emphasize that Lee et al.[49] reported similar observations of a rapid recovery of lithium voids within minutes following delithiation experiments. Please note, that the degree of relaxation may only be minor for very deficient systems and that the diffusion inside of In/Li$_{stacked}$ can be further affected by its geometry (see Section SE, Supporting Information).

In contrast, the impedance spectrum ("after stripping") of In/Li$_{composite}$ shows a drastic impedance increase at 43.6 Ω cm^{-2}, indicating a different cause of polarization. The presence of percolation paths for ions and electrons within the composite enhances lithium replenishment during the delithiation experiment. Consequently, we assume that the blocking behavior of the electrode occurs once most or all active lithium is consumed, and large indium-rich (lithium-ion blocking) or inactive domains prevent subsequent relaxation of the electrode due to increasing tortuosity. We believe that this indicates a significant deterioration of the composite structure, which is preventing a recovery of lithium over time (i.e., the replenishment of lithium). This can be observed in Figure S7 (Supporting Information), indicated by the high impedance at low frequencies. It is important to highlight again that inactive or reacted lithium (e.g., during SEI formation) may persist and the lithium transport in composite electrodes may rely on the particle sizes of each component and their respective ratio.[12]

In order to verify the previous conclusion about the electrode microstructure and resulting impedance contributions, cross sections of both In–Li electrode types were prepared by ion-beam polishing and examined by SEM (**Figures 6** and **7**). Using EBSD, phase and inverse pole figure (IPF) maps of In/Li$_{stacked}$ in pristine (top), plated (middle), and stripped (bottom) state were obtained and are shown in **Figure 6**. Both non-pristine electrodes were extracted from a symmetric cell (In/Li$_{stacked}$|LPSCl|In/Li$_{stacked}$; Figure 3).

In the phase maps, the indium and InLi phase regions are colored purple and yellow, respectively. As expected from above

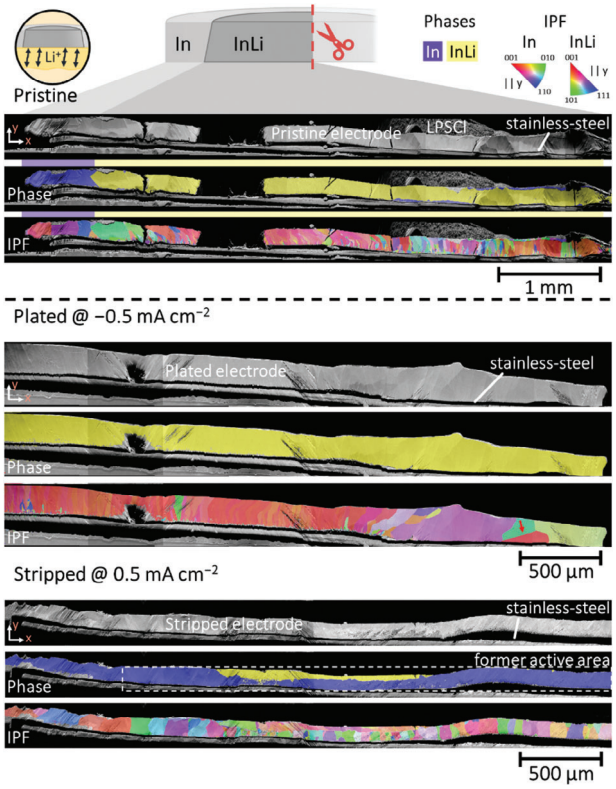

Figure 6. Polished cross sections of $In/Li_{stacked}$ in pristine (top), plated (middle), and stripped state (bottom). SEM images are complemented by phase and IPF maps (given parallel to the y-direction) for indium and intermetallic InLi to reveal their microstructure using EBSD. The WE (stripped) and CE (plated) of unidirectional galvanostatic experiments at 0.5 mA cm^{-2}, 25 °C, and 30 MPa with a cut-off potential of 1 V were studied (Figure 3). For the stripped state, the former active area is approximated and depicted by the dashed rectangular box (white). Parts of the electrodes fell off during sample preparation. One grain exhibiting pseudo-symmetry remains for the plated electrode (marked by a red arrow).[56]

results, and consistent across all samples, no electron backscatter patterns (EBSP) matching the crystal structure of lithium metal were found by the Hough indexing algorithm. IPF maps show the microstructure and grain orientation of both phases parallel to the y-direction. For comparison, a reference measurement of a pristine indium metal foil is provided in Figure S8 (Section SG, Supporting Information).

In the pristine $Li/In_{stacked}$ (top), there is a distinct lateral phase separation between indium metal and InLi. The outer (left) side is composed of indium, while the inner side (right) consists of InLi. This separation is due to the different diameters of the indium and lithium metal foils used during electrode preparation. Consequently, the initial active area is reduced by approximately 1.5 mm in diameter, aligning with our previous assumptions and calculations. Additionally, a thin indium layer (≈20 µm) is visible at the interface to the SE (right side), suggesting an incomplete alloying reaction. A larger magnification of these areas, including selected EBSPs, is added in Figure S9 (Section SH, Supporting Information).

However, since $In/Li_{stacked}$ performed well in the previous tests (Figure 3 and Figure S5, Supporting Information), we consider the effect of such a thin indium layer to be insignificant. Again, we emphasize the importance of matching the thickness of both foils during preparation, as discussed previously. Residuals of lithium metal at the interface to the stainless-steel current collector could not be identified. Examining the IPF map (in y-direction), broad pristine indium grains (up to 100 µm) are observed, while thinner, columnar grains with preferential orientations close to <411> (pink) and <401> (orange) are identified for InLi. The grains of indium at the interface to the SE were smaller (thickness ≈20 µm) and showed a finer microstructure, while the grains of both indium and InLi expanded from the current collector to the SE interface in a columnar shape.[56] In comparison to pristine indium metal foil (Figure S8, Supporting Information), the pre-lithiated InLi grains exhibit a thinner, yet still columnar, shape.

A lithiated $In/Li_{stacked}$ electrode (middle) was analyzed, which served as the CE in Figure 3. The electrode was charged (i.e., lithiated) to nearly ≈99% of its theoretical capacity ($q_{th,lith}$ = 7 mAh cm^{-2}) within the $In/(InLi)_x$ phase field in our study. The phase map indicates a uniform layer growth with the formation of InLi during lithiation, as indium is entirely consumed in the alloying process. This suggests expansion in the active area to access all indium metal (i.e., during the first charging step of full-cells). In fact, we could not localize the former phase boundary of now lithiated indium and pre-lithiated InLi in any map, while we again measured the outer part of the electrode. Higher-lithiated indium alloys, such as In_4Li_5 and In_2Li_3, were not detected. Upon examination of the IPF map, no distinct microstructure was found for the electrochemically-formed InLi phase. Instead, a homogeneously deposited InLi layer and its columnar grain growth in preferential orientations (close to <100>, <030>, and <401>) of the pre-lithiated InLi was observed (pink and orange). The columnar shape of the observed InLi grains appears to be thinner than that of indium, which may be attributed to its moderate homologous temperature at room temperature.

For the stripped electrode (bottom), a bi-layered structure is observed, with InLi at the SE-side and pure indium at the current collector side, consistent with the findings of Jeong et al.[42] Thus, this contrasts with common assumptions that blocking indium layers develop at the SE interface during the early stages of stripping at a moderate rate.[16,34,45] Furthermore, it supports the assumption that the high lithium diffusion within the InLi phase enables gradual delithiation from deeper areas of the electrode, leaving InLi at the interface until high depletion levels are reached.[42] This result also reinforces the conclusion of significant current constriction and reduction in the active area by indium precipitates at the interface at high depletion levels, as observed by the delithiation and impedance measurements (Figures 3 and 5, respectively). The IPF map reveals columnar grains for indium (≈100 µm width), particularly within the delithiated region, restoring a microstructure similar to the pristine indium metal foil (Figure S8, Supporting Information). The remaining InLi grains again show a preferential orientation – similar to the pristine state – close to <411> (pink) and <401> (orange).

In our tests, the intermetallic InLi exhibits a columnar microstructure with grains of thinner sizes compared to indium, while showing preferential orientations across all samples. During plating, the InLi forms in the same preferential orientations

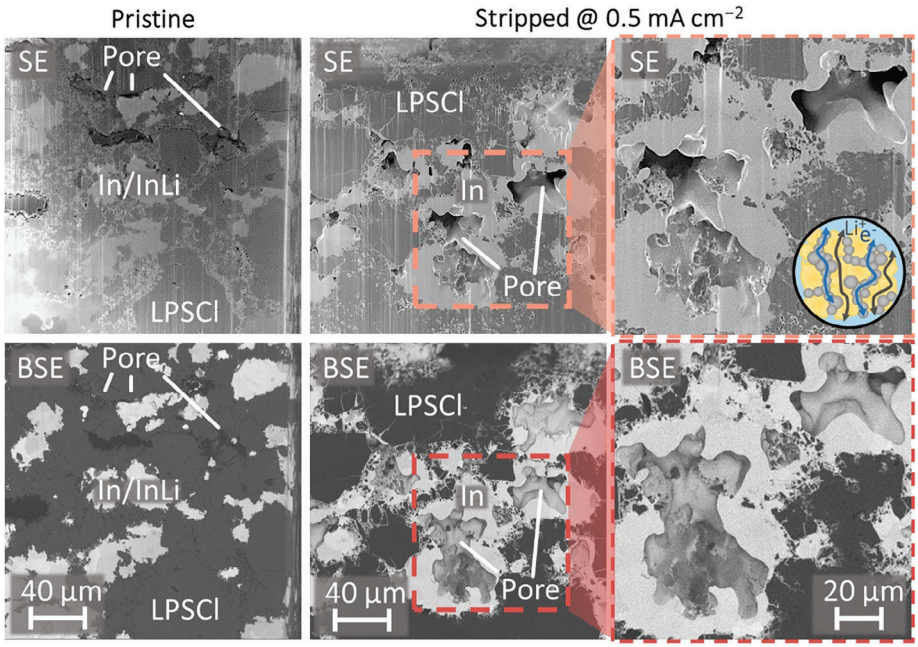

Figure 7. SEM images of a pristine (left) and a fully stripped In/Li$_{composite}$ electrode (middle and right). The cross sections are prepared by focused ion-beam (FIB) milling to reveal the morphology and structure changes after delithiation experiments at 0.5 mA cm^{-2} (cut-off at 1 V), 25 °C, and 30 MPa (Figure 3). The vertical lines observed in the SE imaging are attributed to curtaining effects resulting from the cross section preparation.

as the pre-lithiated InLi. Broad indium grains are obtained during stripping. The incomplete alloying to the interface in the pristine electrode, and the location of residual InLi in the stripped electrode are observed. These observations may be attributed to uneven pressure distribution caused by the stiffness of the InLi phase or other material or preparation inhomogeneities. The electrode thickness changes from its pristine state (≈150 µm) to 170 and 100 µm in the plated and stripped state, respectively. The observed thickness for the plated state is slightly lower than the volumetric predictions based on crystallographic data for the transition from In to InLi.[37]

The combined electrochemical and EBSD results provide strong evidence for: 1) the importance of properly matching both metal foils during cell preparation (see Figure S6, Supporting Information), 2) the minimal impact of inhomogeneous (i.e., incomplete) alloying for the preparation used, 3) the favorable lithium diffusion properties of InLi (i.e., prelithiated electrodes), which improve electrode kinetics and allow access to deeper regions of the electrode, 4) the significant current constriction caused by lithium-deficient indium layers at high depletion levels, and 5) the high accessible capacity during stripping and plating for In/Li$_{stacked}$.

Figure 7 shows the cross sections of In/Li$_{composite}$ in the pristine state (left) and stripped state (middle and right) to reveal the microstructural changes of In/Li$_{composite}$ during stripping. Considering both imaging modes – secondary (SE) and backscattered electrons (BSE) – grain boundaries, morphology details, and material density become evident, respectively. The pristine electrode exhibits a compact structure with only a few irregularly shaped pores (left). The pressure of 380 MPa used for the pristine sample enables high densities. In contrast, the stripped electrode (magnified in the right column) reveals significant pores within the metal fraction of the composite. Hence, this observation indicates a significant deterioration of the composite structure. Moreover, it is worth noting that a smooth morphology of pores is observed. These pores likely indicate the former locations of the InLi phase within the In–Li eutectic or suggest the precipitation of indium on preferred nucleation sites during lithium removal. Apparently, the applied stack pressure of 30 MPa is too low to effectively close the evolving pores during stripping.

Analyzing the material contrasts in the BSE imaging (bottom), three phases are observed in the pristine electrode, while only two phases can be identified for the stripped electrode. In both cases, LPSCl appears significantly darker and it is difficult to distinguish between the brighter particles of In and InLi. This lack of differentiation may be attributed to the effective intermixing or close bulk densities of indium metal and the intermetallic InLi phase (7.31 g cm^{-3} and 5.16 g cm^{-3} (ICSD: 51 960), respectively).

Lastly, it is noteworthy that the non-pristine samples of both electrode types in this microstructural study may not resemble the actual case, if used in full-cell configuration. The nominal CE capacity (here: $q_{th,lith}$ = 7 mAh cm^{-2}) usually exceeds that of the cathode side (i.e., of the CAM), resulting in less phase and volume changes. Moreover, irregularities, inhomogeneities, and incomplete processes during repetitive cycling may further affect the chemomechanical results in full-cell configuration, which we discuss later.

2.4. Reversible Cycling Performance in Full-Cell Configuration

Shifting reference potentials of the CE and significant overpotentials cause early termination of the (dis-)charge process of batteries, and poor capacity utilization. Hence, after

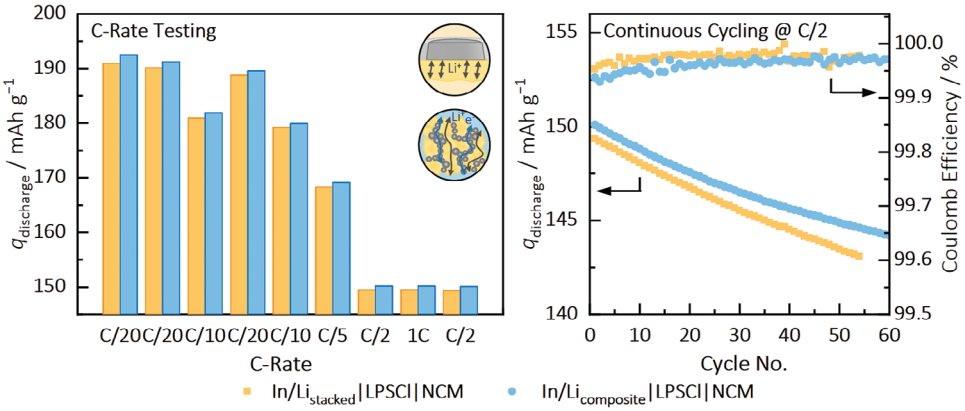

Figure 8. Results of C-rate capability tests, followed by continuous cycling for In/Li$_{stacked}$ (yellow) and In/Li$_{composite}$ (light blue), utilized as CE in fullcell configuration (CE | LPSCl | NCM). Discharge capacities for each cycle at various C-rates (left), as well as the discharge capacities and Coulomb efficiency throughout continuous cycling (right), are presented (one cell for each electrode type, measured at 25 °C and 75 MPa).

assessing the performance under rate-limiting conditions in unidirectional delithiation experiments (Figure 3 and Figure S3, Supporting Information), we advance to evaluate the reversibility and kinetic performance (i.e., overpotentials) of both electrode types in full-cell configuration. Consequently, we employ three different experiments to analyze these important attributes in single cells during galvanostatic cycling. For this, we utilized $LiNi_{0.82}Co_{0.07}Mn_{0.11}O_2$ (NCM) cathode composites (as WEs) with a nominal capacity of 1.85 mAh cm^{-2}, which are referenced to the examined In/(InLi)$_x$ CEs.

First, a C-rate test spanning from C/20 to 1C (corresponding to 0.0925 and 1.85 mA cm^{-2}) was conducted in full-cells (CE | LPSCl | NCM). The results, shown in **Figure 8** (left), indicate high discharge capacities at low C-rates (≈190 mAh g^{-1} at C/20), which decrease with increasing C-rate (≈150 mAh g^{-1} at 1C) for both anode types. Across all rates, slightly higher discharge capacities were achieved with In/Li$_{composite}$.

Second, for a more detailed analysis, the cells were cycled at C/2 (≈0.925 mA cm^{-2}) to assess capacity retention and capacity efficiency during continuous cycling (right). The first ten cycles of the continuous cycling are depicted in Figure S10 (Section SI, Supporting Information). Full-cells with both In–Li anodes exhibited capacity retentions of ≈96 % for the first 55 to 60 cycles. Potential losses may be attributed to volume contraction of NCM, leading to loss of contact and inactive NCM particles, or degradation reactions at the anode and cathode side.[57] Although the results of these tests are mainly focused on the cathode performance, the Coulomb efficiency serves as a first, valuable indicator of the high reversibility and cycling performance of both anodes. For each anode, Coulomb efficiencies exceeding 99.9 % were achieved in each cycle, confirming the suitability of both In–Li anodes at the tested rates for extended cycling durations. Combining all observations, our results are higher or comparable to reports in literature and prove the high capacity utilization and efficiency by both electrode types at various rates and for continuous cycling.

For a more detailed examination of the anode performance, we deconvoluted the contributions of WE and CE using a 3E fullcell configuration (CE | LPSCl | NCM), with a lithiated gold wire serving as the RE.[16,20] Therefore, we monitored the individual potentials of both electrodes in reference to the RE, while performing C-rate tests (as conducted previously). The overpotential of the In–Li CE during cycling for one cycle at each rate (C/20, C/10, and C/5) and five cycles at C/2 is shown in **Figure 9**. The corresponding potentials of the NCM cathode (WE) are presented in Figure S11 (Section SJ, Supporting Information).

For In/Li$_{stacked}$ (left), the overpotential during discharge rose from 8 to 26 mV for C/20 to C/5, respectively. For cycling at C/2 (corresponding to ≈0.925 mA cm^{-2}), the overpotential increased up to 58 mV. During charging, the overpotentials increased from −16 up to −79 mV for C/20 to C/2, respectively. For In/Li$_{composite}$ (right), potential profiles appear smoother and overpotential peaks are reduced, especially during discharge. Nevertheless, the overpotentials during discharge are still very similar to In/Li$_{stacked}$. The charging overpotentials are elevated for low C-rates (−13 to −46 mV for C/20 to C/5, respectively) and slightly reduced (to −76 mV for cycling at C/2). Moreover, these results demonstrate (complementary to the unidirectional galvanostatic measurements), that the anode compositions remain within the In/(InLi)$_x$ two-phase field for the cycled capacity. However, our findings underscore the contrary to common belief, i.e., clear rate limitations by both In–Li anode types at such rates. Thus, this can create an additional performance bottleneck and hinder the accurate benchmarking of cathode performance, particular when it comes to high capacities and rates.

We regard the measured overpotentials of this study as sufficiently low, also compared to the cathode potentials in Figure S11 (Supporting Information), to enable the independent evaluation of solid-state cathodes for the tested current densities. However, we anticipate that increasing rates will lead to substantial overpotentials affecting this task (see Figure S4, Supporting Information). During unidirectional galvanostatic measurements, we consider overpotentials exceeding 100 mV to be concerning. This becomes evident when comparing potential profiles. Significant overpotentials of the CE during the end of charge and discharge processes result in inaccurately referenced WE potentials. This early termination of charging and discharging processes leads to incomplete lithium utilization of the NCM cathode and capacity losses. Considering an overpotential of 100 mV results in capacity losses of 0.4 and 20 mAh g^{-1} for early-terminated

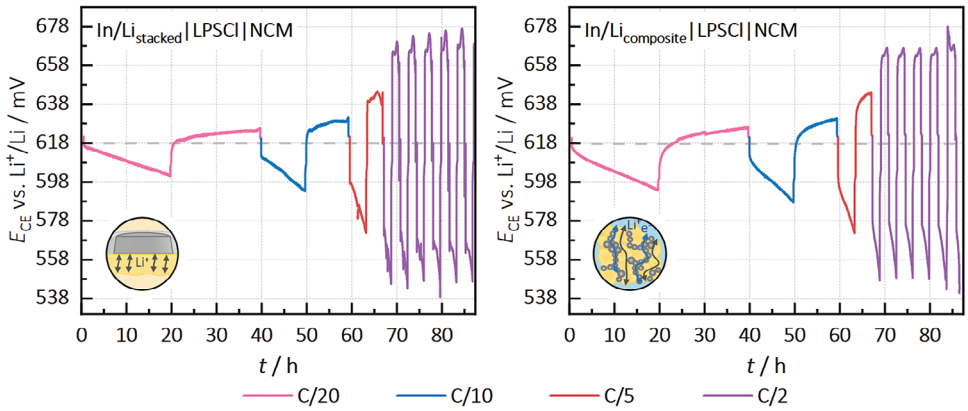

Figure 9. Results of anode kinetic measurements during C-rate capability tests for In/Li$_{stacked}$ (left) and In/Li$_{composite}$ (right), utilized as CE in 3E configuration (CE | LPSCl | NCM with lithiated Au-RE). The CE potential profiles (vs Li$^+$/Li) are presented (one cell for each electrode type, measured at 25 °C and 75 MPa).

discharge and charge processes, respectively. This is also indicated in Figure S10 (Supporting Information). Therefore, appropriate preparation and selection of the CE with suitable kinetics will enhance capacity retention and facilitate the accurate attribution of cathodic effects.

Ikezawa et al.[41] reported similar overpotentials (≈20 mV) for stacked In–Li anodes in full-cell configuration and current densities of ≈0.73 mA cm^{-2} (equivalent 1C in this case). However, they did not provide further information on the Li:In ratio and composition used but observed a significant early termination of (dis-)charging processes, indicating inferior lithium utilization. To the best of our knowledge, Nam et al.[16] first utilized In–Li composites. They reported overpotentials (>100 mV) at low current densities of 0.11 mA cm^{-2}, and even higher overpotentials (>500 mV) at current densities of 1.1 mA cm^{-2}. We attribute these limitations to the low SE content (10–20 wt.%), insufficient ionic percolation paths to deeper regions, and potentially different electrode loadings. Yanev et al.[44] compared In–Li foils and composites and reported overpotentials of up to 250 and 700 mV, respectively, at current densities of 0.28 mA cm^{-2}. However, they noted the early termination of discharge due to increased overpotentials of the foil anode at higher degrees of anode delithiation, whereas it dropped to 20 mV for the composite type. Hence, they consider the composite anode to be more suitable for higher (dis-)charging rates. Concludingly, our results show significantly lower overpotentials for both electrode types at similar or higher (dis-)charging rates compared to reports in literature. However, we could not observe superior kinetics for the composite type used in our tests.

Comparing our results and the available reports in literature, we identify performance variations among electrodes prepared in different laboratories. This is further complicated by inconsistent rate testing, which can lead to misleading conclusions and evaluations across different studies. We emphasize the importance of establishing consistent fabrication and testing protocols, particularly regarding the compositions (In:Li ratio), testing rates, and capacities of In–Li anodes. This is crucial for comparative analysis to better comprehend the mechanisms and kinetics of In–Li electrodes and enhance their suitability as CEs.

Lastly, our objective is to investigate the volume changes of both electrodes during repetitive galvanostatic cycling. Therefore, we analyzed full- cells (CE | LPSCl | NCM) using an uniaxial laboratory press equipped with an active pressure control. This allowed us to maintain constant stack pressure independent of the changes in cell stack thickness during cycling. We opted to utilize NCM as CAM instead of zero-strain materials (such as $Li_4Ti_5O_{12}$) to examine the chemomechanical reversibility of high-voltage full-cells with a high-strain anode. The absolute volume changes of In/(InLi)$_x$ anodes clearly surpass those of NCM.[37,57]

Figure 10 depicts the recorded height changes Δh (top) during galvanostatic cycling (bottom) at C/2 (equivalent to ≈0.925 mA cm^{-2}) for In/Li$_{stacked}$ (left) and In/Li$_{composite}$ (right) for the first five cycles. Unfortunately, continuous high-precision measurements of height changes are hindered by variations in room air-conditioning operation. Considering the height profiles with stable background contributions of a few cycles, the high chemomechanical reversibility observed for ≈40 cycles is remarkable (shown in Figure S12, Section SH, Supporting Information). Jin et al.[35] suggested that porous anode microstructures, evolving during stripping processes, may compensate for volume changes in planar In–Li anodes for LIBs. In our case, the observation of pores and voids inside In/Li$_{composite}$ (as shown in Figure 7) indeed indicates a positive effect on reducing or stabilizing anode height changes. Notably, this result motivates more systematic chemomechanical studies on the characteristics of composite electrodes and the effect of stack pressure (in our case: 75 MPa), potentially closing evolving pores. Consequently, the results of cathode composite studies may support and expedite these efforts for anode composites.[12] For instance, Sakka et al.[58] investigated the influence of pressure on the microstructure (i.e., porosity, contact area, and tortuosity) concerning the electrochemical properties of cathode composites.

Unfortunately, relative height changes (in respect to the initial electrode thickness) are difficult to quantify, especially for the stacked electrode. Despite the background noise, we quantified the absolute height changes by assuming 1D strain, which is constrained by the cell casing. In the cathode composite, the volume fractions of LPSCl and NCM are 61 and 39 vol.% (neglecting carbon additives). Hence, a volume difference of 3%[37,59]

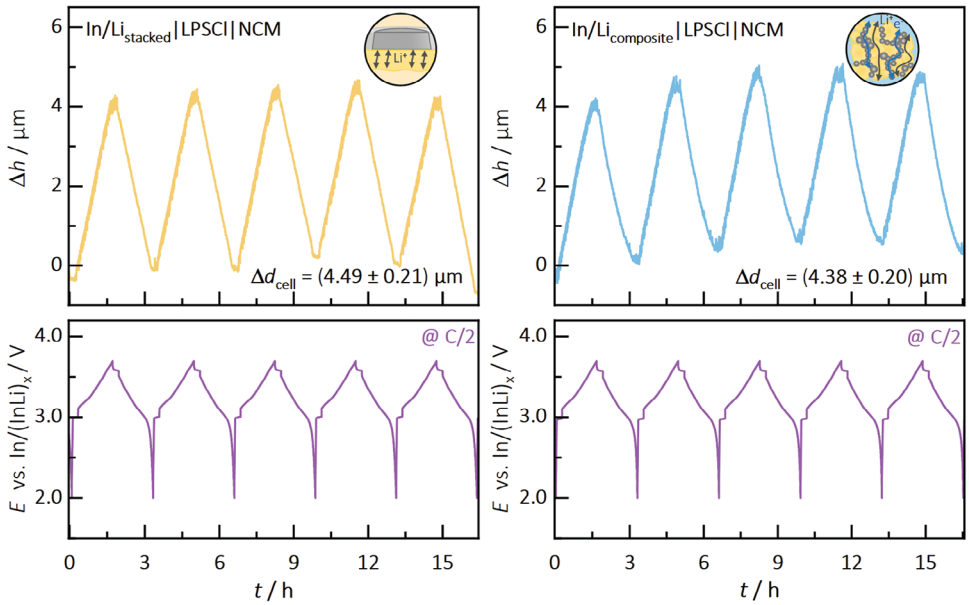

Figure 10. Results of the chemomechanical measurements for continuous cycling at C/2 for In/Li$_{stacked}$ (left) and the In/Li$_{composite}$ (right), utilized as CEs in full-cell configuration (CE | LPSCl | NCM). The height change (Δh, top) and the corresponding full-cell potential profile (vs In/(InLi)$_x$, bottom) are presented for the first five cycles (one cell for each electrode type, measured at 25 °C and 75 MPa).

between charged and discharged states of NCM particles corresponds to a maximal height change of $\Delta d_{NCM} \approx 0.4$ µm. If clearly disturbed cycles (for 40 cycles in Figure S12, Supporting Information) are neglected, the mean height differences ($\Delta d_{In-Li} = \Delta d_{cell} - \Delta d_{NCM}$) of In/Li$_{stacked}$ and In/Li$_{composite}$ result as 3.98 (±0.21) and 4.09 (±0.20) µm, respectively, between charged and discharged states. While these values differ from the theoretical values (≈2.6 µm, calculated from crystallographic data),[37] they are in line with calculations (≈3.9 µm) based on the experimental data of Koerver et al.[57] Apparently, with the setup used and the resolution obtained, we did not observe clear differences between the two electrode types, even though the formation of pores in the particle-based composite electrode could be observed previously. As discussed above, the applied stack pressure may have affected the effective height change of each electrode type. These results highlight the need for high-resolution dilatometry investigations for more precise chemomechanical analysis of electrode materials and composites.

Due to the high chemomechanical reversibility (≈40 cycles, Figure S12, Supporting Information), we anticipate that both In–Li electrodes provide suitable chemomechanics for repetitive cycling in full-cell configuration. The chemomechanical properties of In–Li may even stabilize stack pressure and improve the overall cell performance by counteracting the expansion and shrinkage of NCM particles during cycling.[13,14] We consider the changes in height of ≈4 µm as small to moderate compared to the projected thickness of an optimized SSB cell of ≈150 to 200 µm. However, we suggest that volume changes need to be considered in the evaluation of the cell performance and chemomechanical properties, as it will strongly depend on the type of electrode.

In summary, we observe high reversibility and sufficiently fast electrode kinetics combined with consistent chemomechanical changes during cycling for the two In–Li electrode types tested inside the two-phase eutectic In/(InLi)$_x$. High Coulomb efficiencies, low overpotentials, and predictable volume changes (tested at ≈1 mAh cm^{-2}, C/2) contribute to accurate investigations for ongoing lab-scale studies at moderate capacities, aiding in the advancement of solid-state cathodes. Nevertheless, both In–Li electrode types may require further optimization to align with the (dis-)charge rates of state-of-the-art batteries at 1C (≈3.5 mA cm^{-2}) and with future high-capacity cathodes. Therefore, the transport kinetics (i.e., overpotentials) and rate capabilities need to be adjusted, optimized, and balanced as needed during the anode preparation process.

Both types of electrode rely on the precise adjustment of composition (i.e., the molar ratio of lithium and indium metal),[19] and further optimization may be achieved through systematic variation of geometric parameters. Given its limited potential for adjustment and optimization, we assess the transport kinetics of In/Li$_{stacked}$ as feasible, but only sufficient for modest testing protocols at low to moderate rates and capacities. It is important to highlight the susceptibility to improper kinetics resulting from the selection of different thicknesses for indium and lithium metal. Based on our tests, we recommend using a thickness of 100 µm for both metal foils, with a smaller area allocated for lithium metal. For advanced performance tests, In/Li$_{composite}$ demonstrated its effectiveness in this study, exhibiting slightly lower overpotentials and improved electrochemical as well as chemomechanical reversibility to stabilize testing conditions. This conclusion is further supported by the versatility of the composite type to precisely adjust composition and kinetic performance to individual conditions, starting at a ratio of 60:40 wt.% for In/(InLi)$_x$:SE. These results are in good agreement with the report by Yanev et al.[44] At this point it is important to note, if complete delithiation occurs, a significant deterioration of the composite structure was observed, which has a profound impact on its properties.

Our microstructural analysis of different In–Li anode types, along with reports in the literature, underscores the critical importance of selecting the appropriate types of In–Li anode, understanding the challenges during anode preparation, and recognizing the performance variations among electrodes prepared by different researchers and laboratories. Therefore, this emphasizes the necessity for comprehensive reports in literature, the specified preparation of In–Li anodes, and transparent analysis.[46,50] Notably, solely stating the C-rate without providing the absolute capacity or current density decreases the effective (interlaboratory) comparability of reported values and results. Furthermore, we agree with Aspinall et al.[34] regarding the potential of phase field modeling of the eutectic $In/(InLi)_x$ to provide further insight into the effects of alloy inhomogeneity and spatial lithium deficiencies on electrode kinetics and transport properties. We anticipate that this will contribute to a more refined microstructural understanding of each type of anode, complement our experimental studies, and aid in the establishment of appropriate preparation criteria and guidelines.

3. Conclusion

We compare seven In–Li alloy electrode types within the $In/(InLi)_x$ two-phase field to assess their suitability as electrochemically stable and reliable CEs in the investigation of lab-scale solid-state cathodes. In doing so, we illustrate the specific challenges in preparing both planar and particle-based anodes, highlighting possible errors and the importance of interlaboratory comparison. Through unidirectional galvanostatic experiments we identified the most effective anode types, namely stacking foils of both metals and a mixture of corresponding metallic powders and SE. Both demonstrated effective intermixing, high effective accessibility of lithium, and consistent potential profiles for (dis-)charging rates up to 1.5 mA cm^{-2} (equivalent to capacities of 1.5 mAh cm^{-2} at 1C). Dendrite formation was not observed, even at high current densities of 5 mA cm^{-2}. SEM and EBSD analysis revealed additional insights in the underlying microstructure and the influence of preparation parameters. When used in full-cells, both anodes exhibited good reversibility and sufficiently fast electrode kinetics as CE to facilitate ongoing lab-scale studies at moderate capacities for the advancement of solid-state cathode composites.

High Coulomb efficiencies, low overpotentials (tested at ≈1 mAh cm^{-2}), and predictable volume changes contribute to stable potential referencing and the accurate attribution of cathodic effects in cathode studies. However, the In–Li electrodes evaluated in this study may require further optimization in terms of composition, microstructure and transport properties to match the (dis-)charging rates of state-of-the-art batteries at 1C (≈3.5 mA cm^{-2}) and future high-capacity cathodes. While the stacked foil anode type is simple to prepare, it requires a retention period to ensure proper performance. Composites can be easily tuned and balanced to meet specific requirements (i.e., favorable transport kinetics and high-rate capabilities). Our results highlight the need to optimize the microstructure of eutectic electrodes to keep pace with the continuous improvement of CAMs, SEs and solid-state composites. We emphasize the importance of using the knowledge gained from microstructural studies on cathode composites and studies of the In–Li system to advance anode composites and other intermetallic lithium alloys, respectively.

4. Experimental Section

All experimental procedures were carried out in an argon-filled glovebox (*LabMasterPRO*, MBraun, Garching, Germany), with $p(O_2)/p$ and $p(H_2O)/p < 1$ ppm.

Preparation of In–Li Anodes: Alloys were prepared in the two-phase eutectic phase field $In/(InLi)_x$, which exhibits a constant potential of E_H (vs Li^+/Li) = 0.62 V. In order to achieve comparable performance, every alloying process was tested with 35 at% of lithium (corresponding to $In_{0.65}Li_{0.35}$ or $In_{1-x}/(InLi)_x$ with $x = 0.55$), which was centrally located in the corresponding phase field.[19] In this study, each prepared electrode provides a lithiation capacity $q_{th,lith} = 7$ mAh cm^{-2} and a delithiation capacity $q_{th,delith} = 8.4$ mAh cm^{-2} within the $In/(InLi)_x$ phase field. These capacities correspond to the initial masses of lithium (1.7 mg) and indium metal (51.3 mg), respectively, and were maintained for each electrode type. Figure 1 illustrates each preparation method.

The first type of anode (referred to as "$In/Li_{stacked}$") was prepared by placing lithium foil (100 µm thickness, 6 mm diameter, 99.9 %, China Energy Lithium, China) behind indium foil (100 µm thickness, 9 mm diameter, 99.999 %, ChemPUR, Germany) during cell assembly. This most simple preparation requires the complete dissolution of the lithium into the indium foil, in order to approach the $In/(InLi)_x$ two-phase state.

Direct alloying was tested by two mechanical mixing methods, similar to the works of Dugas et al.[18] and Hennequart et al.[60] Lithium foil was placed between two larger indium sheets and folded repeatedly. After roughly three repetitions it turned dark and stiff, making further processing difficult. Before each folding, the stack was compressed either by a hot press ("$In/Li_{pressed}$") or a calander ("In/Li_{rolled}") at 120 °C. Each resulting foil was then flattened to a thickness of ≈100 µm and anodes with a diameter of 9 mm were punched out.

In–Li anodes made out of powder were prepared by two different preparation methods. Lithium metal powder was synthesized by (droplet) emulsion using an in-house-built setup, as described elsewhere.[61] Indium powder (≈325 mesh, 99.99+ %, abcr, Germany) and lithium metal powder were mixed for 15 min at 15 Hz using a *Pulverisette 23* mini mill (Fritsch, Idar-Oberstein, Germany) and three ZrO_2 balls (5 mm diameter) to obtain a homogeneous In–Li alloy powder ("In/Li_{powder}"). Alloyed In–Li powder ("$In/InLi_{powder}$") was obtained from melt by the same droplet emulsion process. Therefore, the required amount of indium powder was added to the inert medium (prior to lithium metal).

In–Li alloy composite anodes ("$In/Li_{composite}$" and "$In/InLi_{composite}$") were prepared from powders described earlier. Each alloy powder was thoroughly mixed with SE (Li_6PS_5Cl) in a ratio of 60:40 wt.% using a *Pulverisette 23* mini mill (Fritsch, Idar-Oberstein, Germany) in the same way as described earlier. This corresponds to volume fractions of 64.4, 24.2, and 11.4 vol.% for LPSCl, indium, and lithium metal, respectively. Due to the poor control of intermixing and subsequent shifts in local composition, it was opted not to test composite anodes produced by grinding (to powder) of mechanically-mixed anodes.

For current density calculations, an active (anode) area of 0.785 cm^2 was assumed for the sake of simplicity. However, due to the smaller diameter (9 mm) of foil anodes, this may result in slightly higher effective current densities. In unidirectional stripping experiments, the active area might also be further reduced in the case of $In/Li_{stacked}$ anodes, as suggested by the results in Figure 6 and Figure S5 (Supporting Information).

Cell Assembly and Electrochemical Characterization: Lithium argyrodite (Li_6PS_5Cl) SE (POSCO JK Solid Solution Co., Yangsan, South Korea) was used as the separator material and in composites. It exhibited an ionic conductivity of $\sigma_{ion} = 1.1$ mS cm^{-1} at 25 °C. Single-crystalline $LiNi_{0.82}Co_{0.07}Mn_{0.11}O_2$ and carbon nanofibres (CNF) were purchased from MSE Supplies LLC (Tucson, USA), serving as CAM and carbon additive, respectively. A NCM, LPSCl, and CNF mixture (60:37:3 wt.%) was prepared by a *Pulverisette 23* mini mill (as described earlier) and was used as cathode composite for full-cell cycling.

Each cell was prepared by pelletizing 80 mg of solid electrolyte as separator (≈600 µm thickness) in a polyether-ether-ketone casing (10 mm diameter, equipped with stainless steel rods as contacts). Uniaxial pressure of 380 MPa was applied for 3 min at room temperature. To improve contact and densification, each anode and cathode composite was added in advance to the compression step, while each In–Li foil (9 mm diameter) was added afterward. For anode powders and anode composites 53 and 88.3 mg were used as WE, respectively. To ensure consistency, these masses were adjusted to match the lithium capacity (and composition) of the In–Li foils. For the measurement of the (time-dependent) potentials of the different In–Li anodes, Li foil (100 µm thickness, 9 mm diameter) served as CE. For unidirectional galvanostatic experiments, "In/$Li_{stacked}$" anodes were used as the CE due to their simple preparation. 12 mg of cathode composite was used for galvanostatic cycling experiments in full-cell configuration. For measurements of anode kinetics, the electrode potentials were monitored separately during galvanostatic cycling using an in-house-built 3E configuration.[20] One Au-coated tungsten wire (25 µm diameter) was centered inside a 160 mg separator layer before the densification process and served as basis for a µ-RE, as reported by Hertle et al.[20] For chemomechanical investigations during galvanostatic cycling, *CompreCells* (rhd instruments, Darmstadt, Germany) were used and assembled in the same way as described earlier. Here, 114 mg of LPSCl were used due to the larger diameter (12 mm), while the masses and foil dimensions of electrodes remained unchanged.

If not stated otherwise, electrochemical measurements were carried out at 25 °C using a Biologic *VMP 300* potentiostat (BioLogic, Seyssinet-Pariset, France) with a stack pressure of ≈30 MPa applied by external frames. The OCV was recorded for 12 h to monitor the potential of the alloy anodes after preparation. For unidirectional galvanostatic experiments (stripping), current densities of 0.5 mA cm^{-2} with cut-off potentials of 1 V were used. Before each measurement, the OCV was monitored at rest for 5h. For delithiation experiments at 0.5 mA cm^{-2}, electrochemical impedance spectroscopy (EIS) with an amplitude of 10 mV was carried out before and after applying the current. EIS was measured in a frequency range from 3 MHz to 1 Hz. For galvanostatic cycling in full-cell configuration, a series of C-rate capability tests were performed prior to initiating continuous cycling at C/2. These tests included two cycles at C/20, as well as tests at C/10, C/20, C/5, C/2, and 1C for one cycle. Full-cells were cycled in the potential range of 2.0–3.7 V vs In/$(InLi)_x$ and 2.6–4.3 V vs Li^+/Li in 3E configuration. A stack pressure of 75 MPa was applied and for C-rate calculations a theoretical capacity of 200 mAh g^{-1} was assumed for NCM. When employed, the µ-RE initially underwent lithiation for a duration of 16 h, with a current density of 1.25 µA cm^{-2} (using the excess lithium of the In–Li anode). Thereby, a layer of lithium metal was plated onto the gold following a brief Au alloying step. This provides a stable reference potential within the $AuLi_x$/Li phase field (i.e., 0 V vs Li^+/Li). The chemomechanics were investigated by recording the height change during galvanostatic cycling at C/2. Therefore, the uniaxial laboratory press *CompreDrive* (rhd instruments, Darmstadt, Germany), equipped with a high-resolution servo drive for active pressure control (set at 75 MPa in this case), was utilized. For the calculation of corresponding volume ratios in the composite cathode, bulk densities of LPSCl and NCM were assumed to be 1.86 and 4.71 g cm^{-3} (ICSD: 131109 and 34304), respectively.

EBSD and FIB-SEM Measurements: Large-area cross section of foil anodes were first cut by hand and then ion-polished at −110 °C under an inert atmosphere using a triple ion beam cutter (*EM TIC 3X*, Leica Microsystems, Wetzlar, Germany) equipped with three argon-ion guns. Operating conditions were set to 7 kV, a current of ≈2.5 mA, and a polishing time of several hours.

Microstructural characterization was carried out using a *Gemini SEM 560* high-resolution field emission SEM (Carl Zeiss Microscopy GmbH, Oberkochem, Germany), equipped with a *Symmetry 3* EBSD detector (Oxford Instruments, Oxford, UK). The system was operated with the *Aztec 6.1* software package (Oxford Instruments, Oxford, UK). EBSPs were recorded at an excitation voltage of 15 kV and a beam current of 3.3 nA. To achieve optimal pattern quality, exposure time, pattern averaging, background correction, and shadow masking were carefully optimized. Patterns were indexed using a Hough algorithm with a resolution of 60 and 11 bands, considering the phases: tetragonal indium (ICSD 53091), cubic InLi (ICSD 51960), and cubic lithium (ICSD 44367). For mathematical data refinement, the *AZtecCrystal* software package (Oxford Instruments, Oxford, UK) was used to perform wild spikes removal followed by replacing zero solution with six neighbors and pseudo-symmetry removal.

The morphology and structure of composite anodes was investigated by means of FIB milling and SEM using a *XEIA3* (Tescan, Brno, Czech Republic). Therefore, pristine anode composites were compressed at 380 MPa beforehand, while stripped samples were investigated as a former cell stack. For imaging the cross sectional area, a U-shaped trench was milled into the surface and subsequently polished using a xenon plasma ion source. Secondary electron and back-scattered electron SEM images were recorded. In both investigations, sample transfer from the glovebox to the vacuum chamber of the SEM was carried by using the transfer module system *EM VCT500* (Leica, Wetzlar, Germany) to prevent the reaction with moisture and atmosphere.

Supporting Information

Supporting Information is available from the Wiley Online Library or from the author.

Acknowledgements

The authors like to thank Dr. Burak Aktekin and Dr. Till Fuchs for their help in preparing the manuscript and fruitful discussion. C.D.A. and J.J. acknowledge financial support by Bundesministerium für Bildung und Forschung (BMBF) within the ALANO project (Grant No. 03XP0396J). P.M., J.K.E., and J.J. acknowledge the funding by the BMBF within the FestBatt – Cluster of Competence for Solid-State Batteries (Grant No. 03XP0430A). The authors acknowledge the German Research Foundation (DFG) POLiS Cluster of Excellence (Project ID 390874152) for financing of the *CompreDrive* (rhd) device.

Open access funding enabled and organized by Projekt DEAL.

Conflict of Interest

The authors declare no conflict of interest.

Data Availability Statement

The data that support the findings of this study are available from the corresponding author upon reasonable request.

Keywords

alloy anode, cathode composite, electrochemistry, electrode kinetics, electron backscatter diffraction, lithium metal anode, solid-state batteries

Received: September 5, 2024
Revised: November 5, 2024
Published online:

[1] S. Chu, A. Majumdar, *Nature* **2012**, *488*, 294.
[2] D. Larcher, J.-M. Tarascon, *Nat. Chem.* **2015**, *7*, 19.
[3] T. Krauskopf, F. H. Richter, W. G. Zeier, J. Janek, *Chem. Rev.* **2020**, *120*, 7745.

[4] T. Krauskopf, H. Hartmann, W. G. Zeier, J. Janek, *ACS Appl. Mater. Interfaces* **2019**, *11*, 14463.
[5] J. Janek, W. G. Zeier, *Nat. Energy* **2016**, *1*, 16141.
[6] M. J. Wang, E. Kazyak, N. P. Dasgupta, J. Sakamoto, *Joule* **2021**, *5*, 1371.
[7] S. Randau, D. A. Weber, O. Kötz, R. Koerver, P. Braun, A. Weber, E. Ivers-Tiffée, T. Adermann, J. Kulisch, W. G. Zeier, F. H. Richter, J. Janek, *Nat. Energy* **2020**, *5*, 259.
[8] J. Liu, Z. Bao, Y. Cui, E. J. Dufek, J. B. Goodenough, P. Khalifah, Q. Li, B. Y. Liaw, P. Liu, A. Manthiram, Y. S. Meng, V. R. Subramanian, M. F. Toney, V. V. Viswanathan, M. S. Whittingham, J. Xiao, W. Xu, J. Yang, X.-Q. Yang, J.-G. Zhang, *Nat. Energy* **2019**, *4*, 180.
[9] J. C. Bachman, S. Muy, A. Grimaud, H.-H. Chang, N. Pour, S. F. Lux, O. Paschos, F. Maglia, S. Lupart, P. Lamp, L. Giordano, Y. Shao-Horn, *Chem. Rev.* **2016**, *116*, 140.
[10] T. Famprikis, P. Canepa, J. A. Dawson, M. S. Islam, C. Masquelier, *Nat. Mater.* **2019**, *18*, 1278.
[11] J. Janek, W. G. Zeier, *Nat. Energy* **2023**, *8*, 230.
[12] A. Bielefeld, D. A. Weber, J. Janek, *J. Phys. Chem. C* **2019**, *123*, 1626.
[13] P. Minnmann, F. Strauss, A. Bielefeld, R. Ruess, P. Adelhelm, S. Burkhardt, S. L. Dreyer, E. Trevisanello, H. Ehrenberg, T. Brezesinski, F. H. Richter, J. Janek, *Adv. Energy Mater.* **2022**, *12*, 2201425.
[14] R. Ruess, S. Schweidler, H. Hemmelmann, G. Conforto, A. Bielefeld, D. A. Weber, J. Sann, M. T. Elm, J. Janek, *J. Electrochem. Soc.* **2020**, *167*, 100532.
[15] G. Conforto, R. Ruess, D. Schröder, E. Trevisanello, R. Fantin, F. H. Richter, J. Janek, *J. Electrochem. Soc.* **2021**, *168*, 070546.
[16] Y. J. Nam, K. H. Park, D. Y. Oh, W. H. An, Y. S. Jung, *J. Mater. Chem. A* **2018**, *6*, 14867.
[17] C. König, A. Ramanayagam, J. Kraus, B. Roling, *Batteries Supercaps* **2024**, *7*, 202300578.
[18] R. Dugas, Y. Dupraz, E. Quemin, T. Koç, J.-M. Tarascon, *J. Electrochem. Soc.* **2021**, *168*, 090508.
[19] A. L. Santhosha, L. Medenbach, J. R. Buchheim, P. Adelhelm, *Batteries Supercaps* **2019**, *2*, 524.
[20] J. Hertle, F. Walther, B. Mogwitz, S. Schröder, X. Wu, F. H. Richter, J. Janek, *J. Electrochem. Soc.* **2023**, *170*, 040519.
[21] L. M. Riegger, S. Mittelsdorf, T. Fuchs, R. Rueß, F. H. Richter, J. Janek, *Chem. Mater.* **2023**, *35*, 5091.
[22] S. Wenzel, S. J. Sedlmaier, C. Dietrich, W. G. Zeier, J. Janek, *Solid State Ionics* **2018**, *318*, 102.
[23] S. Wenzel, T. Leichtweiss, D. Krüger, J. Sann, J. Janek, *Solid State Ionics* **2015**, *278*, 98.
[24] R. Thümmel, W. Klemm, *Z. Anorg. Allg. Chem.* **1970**, *376*, 44.
[25] W. A. Alexander, L. D. Calvert, R. H. Gamble, K. Schinzel, *Can. J. Chem.* **1976**, *54*, 1052.
[26] K. Takada, N. Aotani, K. Iwamoto, S. Kondo, *Solid State Ionics* **1996**, *86–88*, 877.
[27] M. Tatsumisago, F. Mizuno, A. Hayashi, *J. Power Sources* **2006**, *159*, 193.
[28] C. Wen, R. A. Huggins, *Mater. Res. Bull.* **1980**, *15*, 1225.
[29] Y. Lu, C.-Z. Zhao, R. Zhang, H. Yuan, L.-P. Hou, Z.-H. Fu, X. Chen, J.-Q. Huang, Q. Zhang, *Sci. Adv.* **2021**, *7*, abi5520.
[30] S. Luo, Z. Wang, X. Li, X. Liu, H. Wang, W. Ma, L. Zhang, L. Zhu, X. Zhang, *Nat. Commun.* **2021**, *12*, 6968.
[31] J. Wan, Y.-X. Song, W.-P. Chen, H.-J. Guo, Y. Shi, Y.-J. Guo, J.-L. Shi, Y.-G. Guo, F.-F. Jia, F.-Y. Wang, R. Wen, L.-J. Wan, *J. Am. Chem. Soc.* **2021**, *43*, 839.
[32] J. Qu, J. Xiao, T. Wang, D. Legut, Q. Zhang, *J. Phys. Chem. C* **2020**, *124*, 24644.
[33] C. Hänsel, B. Singh, D. Kiwic, P. Canepa, D. Kundu, *Chem. Mater.* **2021**, *33*, 6029.
[34] J. Aspinall, Y. Chart, H. Guo, P. Shrestha, M. Burton, M. Pasta, *ACS Energy Lett.* **2024**, *9*, 578.
[35] S. Jin, X. Gao, S. Hong, Y. Deng, P. Chen, R. Yang, Y. L. Joo, L. A. Archer, *Joule* **2024**, *8*, 746.
[36] Z. Wang, J. Zhao, X. Zhang, Z. Rong, Y. Tang, X. Liu, L. Zhu, L. Zhang, J. Huang, *eScience* **2023**, *3*, 100087.
[37] W. Zhang, D. Schröder, T. Arlt, I. Manke, R. Koerver, R. Pinedo, D. A. Weber, J. Sann, W. G. Zeier, J. Janek, *J. Mater. Chem. A* **2017**, *5*, 9929.
[38] S. Choudhury, Z. Tu, S. Stalin, D. Vu, K. Fawole, D. Gunceler, R. Sundararaman, L. A. Archer, *Angew. Chem., Int. Ed.* **2017**, *56*, 13070.
[39] European Commission, Directorate-General for Internal Market, Industry, Entrepreneurship, SMEs, M., Grohol, C. Veeh: Publications Office of the European Union, **2023**.
[40] P. Oh, J. Yun, J. H. Choi, K. S. Saqib, T. J. Embleton, S. Park, C. Lee, J. Ali, K. Ko, J. Cho, *Angew. Chem.* **2022**, *134*, 202201249.
[41] A. Ikezawa, G. Fukunishi, T. Okajima, F. Kitamura, K. Suzuki, M. Hirayama, R. Kanno, H. Arai, *Electrochem. Commun.* **2020**, *116*, 106743.
[42] W. J. Jeong, C. Wang, S. G. Yoon, Y. Liu, T. Chen, M. T. McDowell, *ACS Energy Lett.* **2024**, *9*, 2554.
[43] S. Lu, X. Zhang, Z. Yang, Y. Zhang, T. Yang, Z. Zhao, D. Mu, F. Wu, *Nano Lett.* **2023**, *23*, 56.
[44] S. Yanev, C. Heubner, K. Nikolowski, M. Partsch, H. Auer, A. Michaelis, *J. Electrochem. Soc.* **2024**, *171*, 020512.
[45] C. Sedlmeier, R. Schuster, C. Schramm, H. A. Gasteiger, *J. Electrochem. Soc.* **2023**, *170*, 030536.
[46] S. Puls, E. Nazmutdinova, F. Kalyk, H. M. Woolley, J. F. Thomsen, Z. Cheng, A. Fauchier-Magnan, A. Gautam, M. Gockeln, S.-Y. Ham, M. T. Hasan, M.-G. Jeong, D. Hiraoka, J. S. Kim, T. Kutsch, B. Lelotte, P. Minnmann, V. Miß, K. Motohashi, D. L. Nelson, F. Ooms, F. Piccolo, C. Plank, M. Rosner, S. E. Sandoval, E. Schlautmann, R. Schuster, D. Spencer-Jolly, Y. Sun, B. S. Vishnugopi, et al., *Nat Energy* **2024**, *9*, 1310.
[47] J. K. Eckhardt, T. Fuchs, S. Burkhardt, P. J. Klar, J. Janek, C. Heiliger, *ACS Appl. Mater. Interfaces* **2022**, *14*, 42757.
[48] J. K. Eckhardt, T. Fuchs, S. Burkhardt, P. J. Klar, J. Janek, C. Heiliger, *Adv. Mater. Interfaces* **2023**, *10*, 2202354.
[49] K. Lee, E. Kazyak, M. J. Wang, N. P. Dasgupta, J. Sakamoto, *Joule* **2022**, *6*, 2547.
[50] N. M. Vargas-Barbosa, *Nat. Nanotechnol.* **2024**, *19*, 419.
[51] G. V. Alexander, C. Shi, J. O'Neill, E. D. Wachsman, *Nat. Mater.* **2023**, *22*, 1136.
[52] P. W. Jaschin, C. R. Tang, E. D. Wachsman, *Energy Environ. Sci.* **2024**, *17*, 727.
[53] T. Krauskopf, B. Mogwitz, C. Rosenbach, W. G. Zeier, J. Janek, *Adv. Energy Mater.* **2019**, *9*, 1902568.
[54] M. Siniscalchi, J. Liu, J. S. Gibson, S. J. Turrell, J. Aspinall, R. S. Weatherup, M. Pasta, S. C. Speller, C. R. M. Grovenor, *ACS Energy Lett.* **2022**, *7*, 3593.
[55] J. Aspinall, K. Sada, H. Guo, S. Kotakadi, S. Narayanan, Y. Chart, B. Jagger, E. Milan, L. Brassart, D. Armstrong, M. Pasta, *Nat. Commun.* **2024**, *15*, 4511.
[56] T. Fuchs, T. Ortmann, J. Becker, C. Haslam, M. Ziegler, V. Singh, M. Rohnke, B. Mogwitz, K. Peppler, L. Nazar, J. Sakamoto, J. Janek, **2024**.
[57] R. Koerver, W. Zhang, L. de Biasi, S. Schweidler, A. O. Kondrakov, S. Kolling, T. Brezesinski, P. Hartmann, W. G. Zeier, J. Janek, *Energy Environ. Sci.* **2018**, *11*, 2142.
[58] Y. Sakka, H. Yamashige, A. Watanabe, A. Takeuchi, M. Uesugi, K. Uesugi, Y. Orikasa, *J. Mater. Chem. A* **2022**, *10*, 16602.
[59] L. de Biasi, A. O. Kondrakov, H. Geßwein, T. Brezesinski, P. Hartmann, J. Janek, *J. Phys. Chem. C* **2017**, *121*, 26163.
[60] B. Hennequart, M. Platonova, R. Chometon, T. Marchandier, A. Benedetto, E. Quemin, R. Dugas, C. Lethien, J.-M. Tarascon, *ACS Energy Lett.* **2024**, *9*, 454.
[61] C. D. Alt, N. U. Müller, L. M. Riegger, B. Aktekin, P. Minnmann, K. Peppler, J. Janek, *Joule* **2024**, *8*, 2755.